# 27
# CO Clean-up: Preferential Oxidation

*Xun Ouyang and Ronald S. Besser*

## 27.1
## Introduction

An essential requirement for low-temperature polymer–electrolyte–membrane fuel cells (PEMFCs) is the deep removal of CO from the reformate stream after fuel reforming and water gas shift (WGS) reactions. This process must reduce CO from 0.5–1.0% to below 10 ppm with minimum $H_2$ consumption. This CO polishing step can be achieved through different processes, including preferential oxidation (PrOx), selective methanation, pressure swing adsorption (PSA) and $H_2$ membrane technology. Although more than 99% $H_2$ can be obtained and one or more WGS steps can be eliminated with the last two routes, both technologies require high-pressure operation, typically above 5 bar [1], which imposes penalties on material and balance-of-plant costs and startup time. Further, these technologies become prohibitive in fuel processors adopting autothermal reforming or catalytic partial oxidation reforming, where a high-pressure air compressor is necessary. Selective methanation is an attractive option since this is a low-pressure process that does not require air supplies. However, several studies [2, 3] have indicated that this process tends to be unstable even under intensive temperature control to prevent temperature run-away and undesired $CO_2$ methanation. In comparison, PrOx does not require elevated pressure and temperature run-away can be prevented through air flow regulation. Hence PrOx is generally considered the most favorable CO cleanup approach due to its advantages over other technologies. A fuel processor with different CO cleanup schemes is shown in Figure 27.1.

The research interest in PrOx has mainly focused on different catalyst systems. Pt/$Al_2O_3$ has been the most studied PrOx catalyst because of its high CO conversion and stability at moderate temperatures. A maximum CO conversion at 200 °C with a selectivity of ~40% was reported by different groups [4–8]. The general consensus was made that two reaction regimes exist before and after light-off, including a low oxidation rate with a high $CO_2$ selectivity regime and a high rate regime but with low $CO_2$ selectivity. In addition, it was agreed that $O_2$ adsorption is the limiting step

*Micro Process Engineering, Vol. 2: Devices, Reactions and Applications.*
Edited by V. Hessel, A. Renken, J.C. Schouten, and J.-I. Yoshida

ISBN: 978-3-527-31550-5

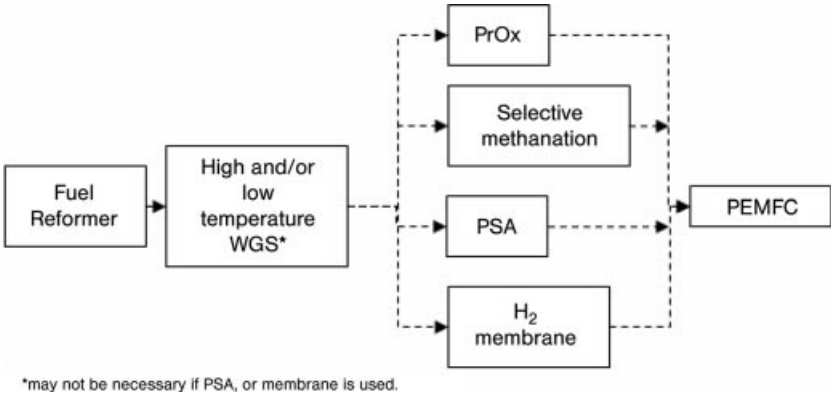


**Figure 27.1** The fuel processor with different CO cleanup schemes.

before light-off [4–9], which can be affected by various factors, e.g. the Pt particle size [10], the $H_2O$ and $H_2$ concentrations in the reactant stream [4] and catalyst preparation methods [11]. In order to improve the PrOx reaction activity at lower temperatures (<150 °C), Farrauto and coworkers [12, 13] and Roberts *et al.* [14] explored $Pt/Al_2O_3$ promoted with iron oxide, which provides independent $O_2$ adsorption sites and hence increases the CO oxidation activity at low temperatures. Other noble metals, such as Ru [6, 15], Au [16, 17], metal oxide [18] and bimetallic catalysts [19], were also investigated.

Until recently, most PrOx studies have been based on packed-bed laboratory reactors which are susceptible to mass and heat transport limitations [20, 21] due to the exothermic nature of this reaction system. A literature survey of PrOx kinetic studies on $Pt/Al_2O_3$ revealed a large discrepancy in turnover frequency calculations under similar process conditions [22], which was believed to be caused by different degrees of transport limitation within the test reactors. Therefore, practical PrOx reactor designs often adopt small catalyst particles (~50 μm radius) to minimize the mass transport resistance [4] and multi-stage heat-exchange reactor systems [23] to prevent hot-spot formation. However, these designs impose an efficiency penalty and increase the system complexity, and further studies have shown that heat transport can still be a limiting factor [22, 24]. Microreactors, especially with thin-film catalyst coatings, are generally accepted to have superior mass and heat transport properties due to their extremely small critical dimensions. Along with their advantages of integration flexibility and small footprint, they are ideal tools for intrinsic reaction kinetic studies and strong candidates for PrOx reactors and portable fuel processors in general.

## 27.2 PrOx Kinetics

Three reactions are important within the operating conditions of PrOx, namely the desired CO oxidation and the undesired $H_2$ oxidation and reverse water gas shift

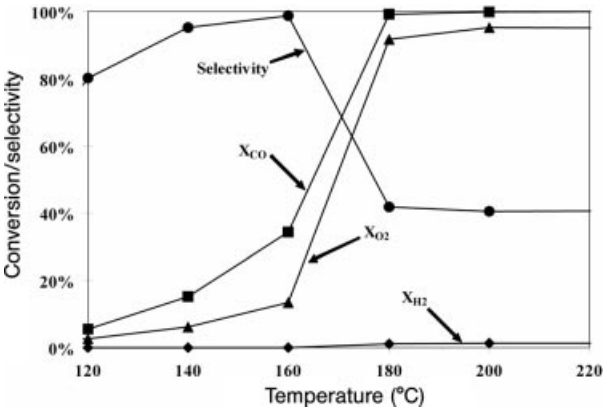


**Figure 27.2** Characteristic PrOx behavior on $Pt/Al_2O_3$ [22].

(r-WGS) reaction (Equations 27.1–27.3). The characteristic PrOx behavior is shown in Figure 27.2. At low temperatures before light-off, both CO and $H_2$ conversions are low with high $CO_2$ selectivity. Higher temperature leads to the light-off of CO oxidation, followed immediately by $H_2$ oxidation. Subsequently, $CO_2$ selectivity drops drastically. On the other hand, the $O_2$ conversion is low before CO oxidation light-off, but essentially complete after the light-off.

$$CO + \frac{1}{2}O_2 \xrightarrow{\Delta H = -67 \text{ kcal mol}^{-1}} CO_2 \tag{27.1}$$

$$H_2 + \frac{1}{2}O_2 \xrightarrow{\Delta H = -58 \text{ kcal mol}^{-1}} H_2O \tag{27.2}$$

$$CO_2 + H_2 \xrightarrow{\Delta H = 9.8 \text{ kcal mol}^{-1}} CO + H_2O \tag{27.3}$$

Most reported PrOx kinetic studies have focused on the CO oxidation [25–27] and neglected the influence of r-WGS reaction [28]. However, the incorporation of rate expressions of the coupled $H_2$ oxidation and r-WGS reactions is necessary for accurate representation of PrOx reaction behavior. Despite the importance of the evaluation of all three expressions, only a few groups have addressed kinetic expressions for all three PrOx reactions [29]. As an example, based on the observation of characteristic PrOx behavior and other PrOx kinetic studies in the literature [29], the kinetic expressions for PrOx on $Pt/Al_2O_3$ are as shown in Equations 27.4–27.9.

$$r_1' = \frac{k_1 P_{CO} P_{O_2}}{(1 + K_1 P_{CO})^2} \tag{27.4}$$

$$r_2' = k_2 P_O^{\beta_1} P_{H_2}^{\beta_2} P_{CO}^{\beta_3} \tag{27.5}$$

$$r_3' = k_3 \left( \frac{P_{CO_2} P_{H_2}}{K_3} - P_{CO} P_{H_2O} \right) \tag{27.6}$$

$$k_i = A_i \exp\left(-\frac{E_i}{RT}\right), \quad i = 1, 2, 3 \tag{27.7}$$

$$K_1 = K_1^0 \exp\left(\frac{\Delta H_{\text{ads}}}{RT}\right) \tag{27.8}$$

$$K_3 = \exp\left(\frac{4577.8}{T} - 4.33\right) \tag{27.9}$$

The power law expression was widely adopted in the literature for CO oxidation [25–27]. This form is simplified from a Langmuir–Hinshelwood (L–H) expression and not suitable for small CO concentrations [30]. Therefore a full L–H expression for CO oxidation is necessary to account for a wide range of CO concentrations (Equation 27.4). The $H_2$ oxidation was previously modeled using empirical power law rate expressions by others [29]. However, in PrOx in the presence of CO, the rate-limiting CO desorption strongly inhibits $H_2$ and $O_2$ adsorption and the subsequent $H_2$ oxidation. Hence the incorporation of $P_{CO}$ in the $H_2$ oxidation rate expression is necessary (Equation 27.5). The kinetics of the r-WGS reaction were well studied previously [31], in which an empirical reversible rate expression [32] is attractive due to its relative simplicity and its appropriateness in PrOx kinetic studies, as demonstrated previously [29].

## 27.3 PrOx in Microreactors

PrOx has attracted much attention from the microreactor community mainly for two reasons, (1) the extremely fast kinetics and exothermicity, which challenge the accuracy of conventional kinetic tools, and (2) the interest in compact and integrated portable fuel cell systems. This section is therefore organized according to these two categories. Since an earlier review on PrOx in microreactors was presented by Kolb *et al.* [33], the purpose of this section is to extend that review with new updates.

### 27.3.1 Microreactors as Tools for Catalyst and Kinetic Studies

#### 27.3.1.1 Catalyzed Microstructured Reactors for PrOx Catalyst Screening [33,34]

Within the European Union-funded project MiRTH-e [35] to design a 100 W methanol fuel processor, a PrOx microchannel reactor system was developed to evaluate nine different PrOx catalyst candidates (Figures 27.3 and 27.4). The incipient wetness impregnation method was used to immobilize the catalyst layers in the microchannels. The average thickness of the catalyst was ca. 40 μm. These catalyst samples were studied for kinetic activity, the effect of $O_2$:CO ratio, the effect of $H_2O$, the effect of space velocity and long-term testing. They found that Pt–Ru/γ-$Al_2O_3$, Rh/γ-$Al_2O_3$ and Pt–Rh/γ-$Al_2O_3$ are the most active candidates with the last being the

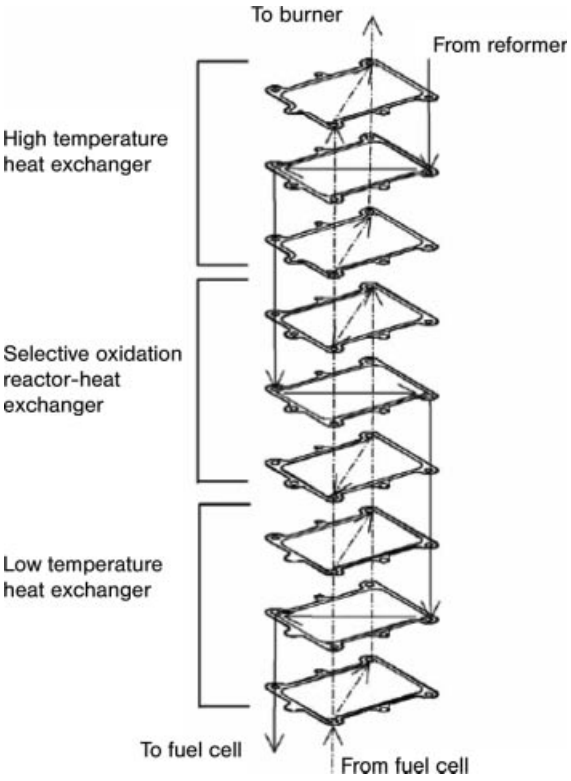


**Figure 27.3** The flow path within the microreactor that was used in the MiRTH-e project.

most stable. At the end of a 50 h test on this catalyst, the CO concentration was below 20 ppm with an $O_2$:CO ratio of 4 and a gas hourly space velocity (GHSV) of 15 500 $h^{-1}$. The product concentration temperature characteristic was then studied with the Pt–Rh/γ-$Al_2O_3$ catalyst. Under the process conditions of an $O_2$:CO ratio of 4 and a

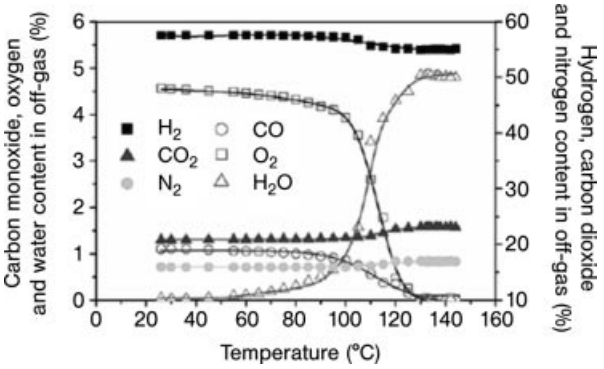


**Figure 27.4** PrOx product composition versus temperature at an $O_2$:C ratio of 4 and a GHSV of 15 500 $h^{-1}$ over a Pt–Rh/γ-$Al_2O_3$ catalyst.

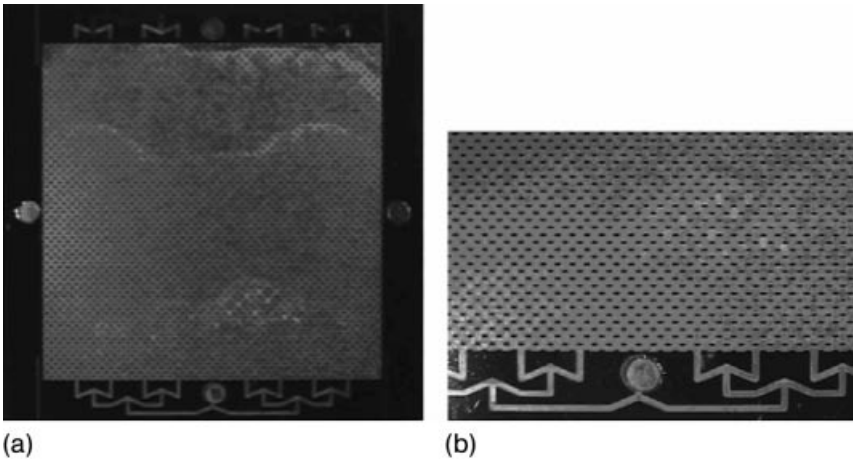


**Figure 27.5** Photographs of the Si microreactor with microposts.

GHSV of 15 500 $hr^{-1}$, a reformate stream for a 28 $W_e$ fuel cell was then produced with less than 10 ppm CO.

27.3.1.2 **Silicon Microfabricated PrOx Reactor with Washcoated Microposts** [36]
Work at the University of Michigan [36] compared a thin-film catalytic microreactor with a packed-bed microreactor using PrOx as a model reaction system (Figure 27.5). The purpose was to study whether external mass transfer resistance for the thin-film catalytic system is a limiting factor. Silicon microreactors with rows of pillars of $200 \times 400\,\mu m$ characteristic dimensions were washcoated with 2% $Pt/Al_2O_3$ catalyst. The catalyst was prepared with a slurry–sol hybrid suspension followed by a syringe injection. With repetition of coating and drying steps and the last calcination step, the final thin-film catalyst thickness was ca. 10 μm. This microreactor was studied in comparison with a packed-bed microreactor of 4 mm i.d. × 8 mm bed height and 62 μm particle size. The authors estimated that both types of microreactors have similar internal diffusion length and negligible heat transfer resistance due to the relatively low space velocities. Consequently, by comparing their reaction results, the effect of external heat transfer could be determined. A 1D diffusion equation was first used to estimate the characteristic gas diffusion time of the microchannel, indicating insignificant external mass transfer resistance. Two-dimensional CFD models were used to confirm good mixing at the reactor entrance region and low heat transfer resistance. In the experiment to study CO, $O_2$ conversion and $CO_2$ selectivity at different temperatures, the performances of the two types of reactors were close to each other, indicating the external mass transfer of the thin-film catalyzed system is not a limiting factor for the PrOx reaction.

27.3.1.3 **Improved PrOx Performance Versus Monolith** [37]
A group at the Dalian Institute of Chemical Physics (DICP) in China [37] studied a potassium-promoted $Rh–K/Al_2O_3$ catalyst microchannel plate reactor with critical

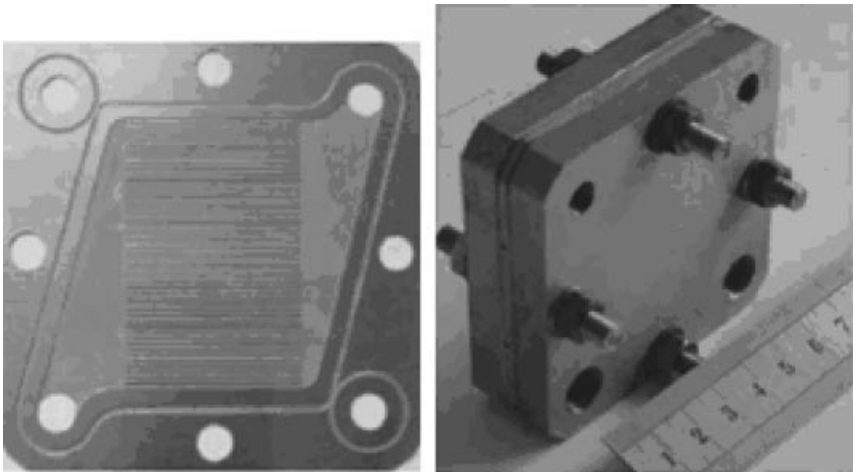

**Figure 27.6** The microchannel reactor used by DICP in the PrOx study with Rh–K/$Al_2O_3$ catalyst.

dimensions of 170 × 500 µm (Figures 27.6 and 27.7). The same catalyst was first studied on a monolith substrate, which showed significant methane production at a relatively low reactor control temperature, indicating internal hot-spot formation due to severe heat transfer limitation. With the same catalyst formulation, methane formation was an order of magnitude lower in the microchannel reactor compared with the monolith. In addition, the microreactor showed a significantly higher CO conversion than the monolith at the same GHSV, again revealing the ultra-fast transport properties of the microreactor.

27.3.1.4 **PrOx Study with Grooved Stainless-steel Foils and Au-based Catalysts** [38]
Another investigation to study PrOx catalyst activity and to examine heat transfer properties was performed by the Institute for Micro Process Engineering (IMVT) [38] using microreactors with grooved stainless-steel foils (Figures 27.8 and 27.9). The

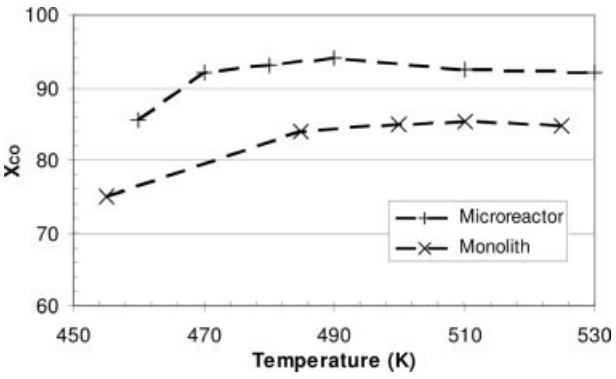


**Figure 27.7** CO conversion versus temperature in the microreactor and the monolith reactor at a GHSV of 300 000 $h^{-1}$.

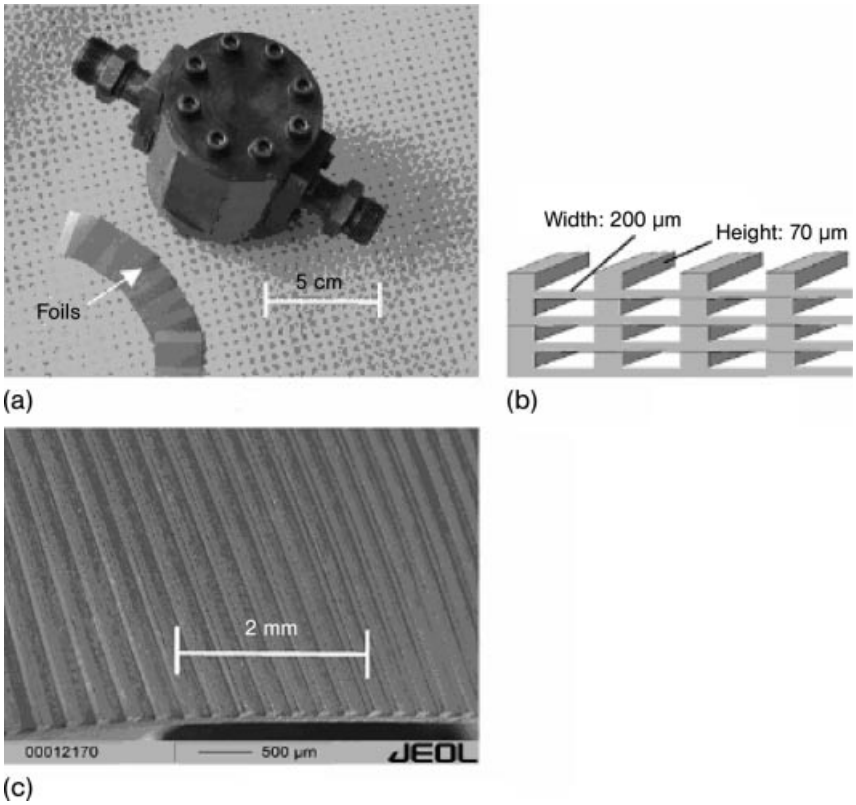


**Figure 27.8** (a) Clamping device for testing the coated foils concerning the WGS and the PrOx reactions; (b) scheme of stacked foils; (c) microstructured foil.

geometric features of the foils include $200 \times 70\,\mu m$ channels and 25 foils clamped together to form the microreactor. Three catalyst recipes, Au/$\alpha$-$Fe_2O_3$, CuO/$CeO_2$ and Au/$CeO_2$-II, were impregnated inside the microreactors for test purposes. Experiments showed that the Au/$CeO_2$-II-catalyzed microreactor has the highest activity, reaching a maximum CO conversion of 79% at 200 °C. Finally, a wider operating temperature window (60–180 °C) was found with the microreactor compared with other studies with conventional reactors based on similar catalyst recipes (60–120 °C) [39, 40], thus demonstrating the high heat transfer efficiency of the microreactor.

### 27.3.2
### PrOx in Integrated Fuel Processors

#### 27.3.2.1 A 2.4 $W_e$ Micro Fuel Processor Based on Microchannels [41–43]

Casio Computer has developed a 2.4 $W_e$ integrated micro fuel processor comprising a methanol steam reformer, a PrOx reactor and a catalytic combustor (Figures 27.10

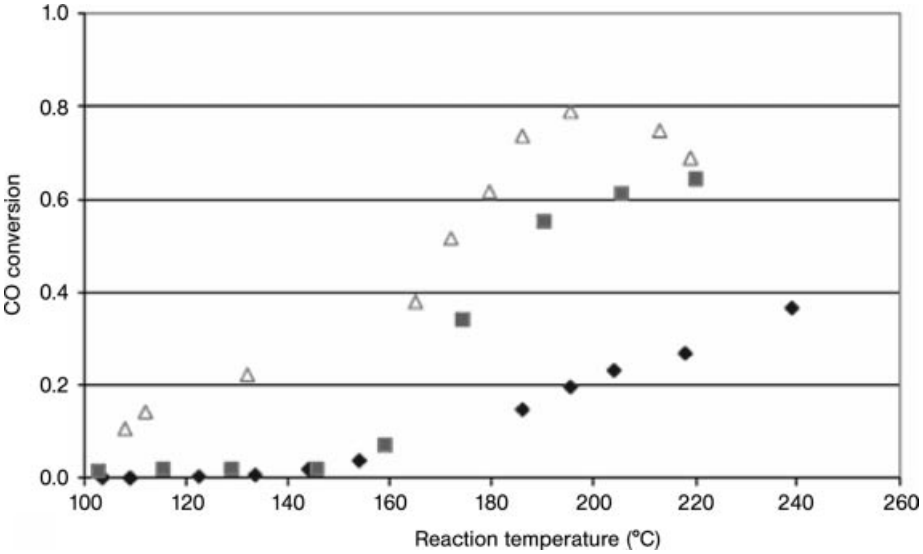


**Figure 27.9** CO conversion versus temperature of the three catalysts tested with the microreactor with an inlet CO concentration of 8% and a residence time of 14 ms. ◆, $Au/Fe_2O_3$; ■, $Au/CeO_2$-II; Δ, $CuO/CeO_2$.

and 27.11). In this device, Pd/ZnO was chosen as the steam reforming catalyst and $Pt/Al_2O_3$ as both the PrOx and catalytic combustion catalysts. Specifically, the PrOx catalyst was coated as a 25 μm thick film in a $1.6 \times 1.5 \times 100$ mm channel. The microchannels were etched in three glass sheets by sandblasting and closed by anodic bonding after catalyst deposition. Cylindrical glass tubes were used for interconnections, which were packaged with a low melting point frit. Patterned Au thin films were coated on the middle glass sheet as electric heaters and temperature sensors.

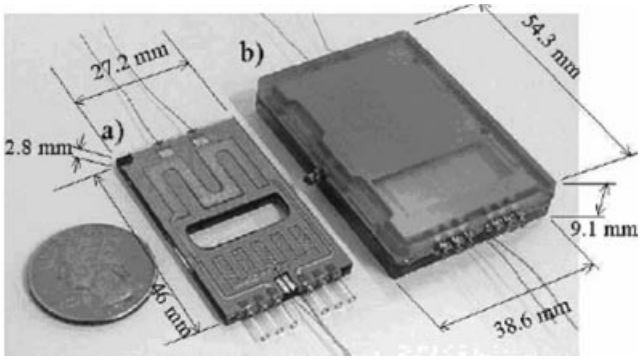


**Figure 27.10** A photograph of (a) the 2.4 $W_e$ micro fuel processor developed by Casio Computer and (b) vacuum package enclosing the microreactor.

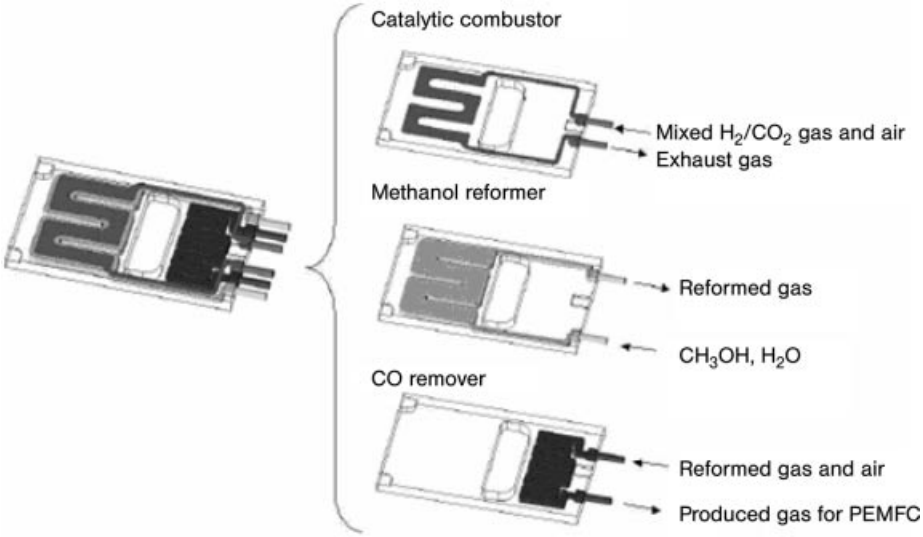


**Figure 27.11** Layered structure of catalyzed microchannel reactor.

Optimal thermal management was achieved by applying a combination of vacuum packaging and metal heat bridges between the high-temperature (i.e. steam reforming and catalytic combustion) and the low-temperature PrOx zones. Vacuum packaging was also used to insulate the device from the ambient. The overall design was verified with CFD and FEM simulations.

Due to the extremely small thermal mass and excellent insulation of the device, a startup time of less than 5 s brought the reforming/combustion zone to 260 °C and the PrOx zone to 110 °C. An individual PrOx reactor test showed less than 10 ppm CO within a temperature window of 110–140 °C. During integrated operation, with the CO exiting the steam reformer at ca. 1%, the CO level following the PrOx reactor was less than 50 ppm.

#### 27.3.2.2 **Microchannel Reactors for a 100 $W_e$ Portable Fuel Processor** [44,45]

In the MiRTH-e project, a methodological approach was adopted for the design, modeling and operation of a PrOx heat-exchange microdevice for a 100-$W_e$ portable fuel processor (Figures 27.12–27.14 and Table 27.1). The device is composed of three countercurrent heat exchangers in series with the middle heat exchanger as the PrOx reactor. The PrOx reactor has a decreasing temperature profile to take advantage of the high activity at the beginning portion of the reactor and high selectivity at the latter portion. Thin-film Pt–Ru/$Al_2O_3$ catalyst was applied to form a 50 μm layer. Stainless-steel plates of 500 μm thickness were etched to form different channel dimensions as summarized in Table 27.1. The reactor was formed with numerous etched plates welded together. The microreactor design was rationalized as follows. A 3D CFD model was first used to study geometry impacts followed by a 2D model to study heat transfer. Finally, a 1D model combining the previous two results was

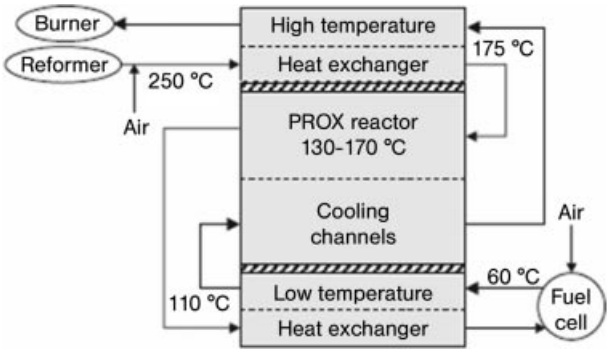


**Figure 27.12** Schematic of the integrated PrOx heat-exchange microdevice.

constructed for comprehensive studies of the integrated device. The modeling results were validated with later experimental data. The experimental results showed acceptable performance with slow deactivation for the first 80 h but rapid deactivation afterwards. The deactivation mechanism was not clear but a higher catalyst loading seems to be necessary with this catalyst recipe and the flow conditions. The heat recovery efficiency of the device seemed to be excellent, providing room to reduce the insulation volume. Due to the small size and its inherent small thermal mass, the transient-response study showed excellent performance with a 4 min time constant.

#### 27.3.2.3 **A 100 $W_e$ Gasoline Fuel Processor Based on Foam Structure with Micropores** [46]

A study of a 100 $W_e$ gasoline fuel processor was carried out at the University of Michigan in a US Department of Energy-funded program. The system under study involved desulfurization, autothermal reforming, WGS and PrOx reactions (Figure 27.14). All reactors were based on the same microreactor design, as shown in Figure 27.14. FeCrAiY metal foams with 80 pores per inch (ppi) were used as the catalyst support, implying a characteristic dimension of ca. 300 μm. The foam

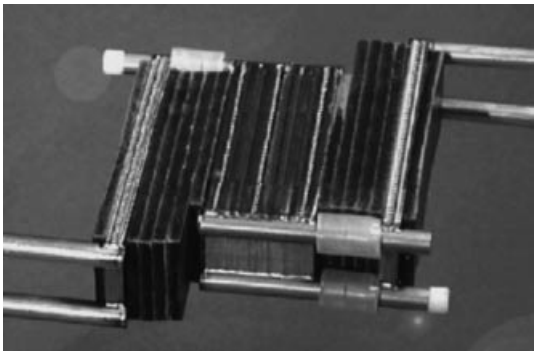

**Figure 27.13** A photograph of the integrated PrOx heat-exchange microdevice.

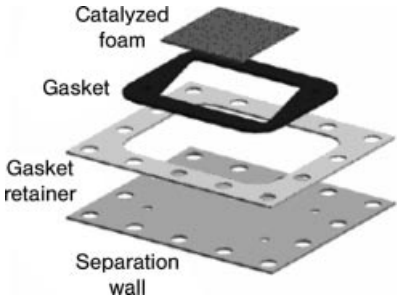


**Figure 27.14** Schematic drawing of the microreactor structure.

supports were adopted because they promote high surface area, large void fraction (i.e. low pressure drop), high thermal conductivity and local mixing. Each of the two stages of the PrOx reactor incorporated 15 foam pieces with each supporting 1.2 g of $Pt/Al_2O_3$ catalyst. Operating at 200 and 140 °C for the first and second stages, respectively, CO in the reformate was reduced from 0.8% to below 5 ppm. The power density was calculated to be $8.333\,W_t\,L^{-1}$ compared with the DOE target of $9.091\,W_t\,L^{-1}$.

#### 27.3.2.4 **A 2 $kW_e$ Multistage PrOx Microchannel Reactor** [47]

A four-stage PrOx microchannel heat-exchange reactor was made by Pacific Northwest National Laboratory (PNNL) to evaluate the potential importance of microchannel architectures in reducing size and weight and improving performance (Figures 27.15 and 27.16). This is also an example of a large-scale system based on microchannels. The first three stages were coated with non-precious metal catalysts and the last with a precious metal catalyst. A microchannel heat exchanger was used for heat removal of all four PrOx stages. The PrOx reactor was operated at the 2 $kW_e$ level, reducing CO from 1% to below 10 ppm. Moreover, the microreactor system required an $O_2$ CO ratio of only 1.2 at a high GHSV of $93\,000\,h^{-1}$, which the authors attributed to the superior thermal management of the system.

**Table 27.1** Specifications of low- and high-temperature heat exchangers and the PrOx reactor.

| | Heat exchangers[a] | | PrOx reactor[a] | |
|---|---|---|---|---|
| **Parameter** | **Ref.** | **Cool.** | **Ref.** | **Cool.** |
| Plate dimensions (width × length) (mm) | 17 × 50 | | 17 × 40 | |
| Number of plates | 2 | 4 | 22 | 11 |
| Channels per plate | 29 | 29 | 13 | 10 |
| Channel width (μm) | 400 | 400 | 1000 | 500 |
| Channel height (μm) | 300 | 300 | 200 | 250 |
| Channel length (mm) | 40 | 40 | 30 | 30 |

[a]Ref. = reformate side, cool. = coolant side.

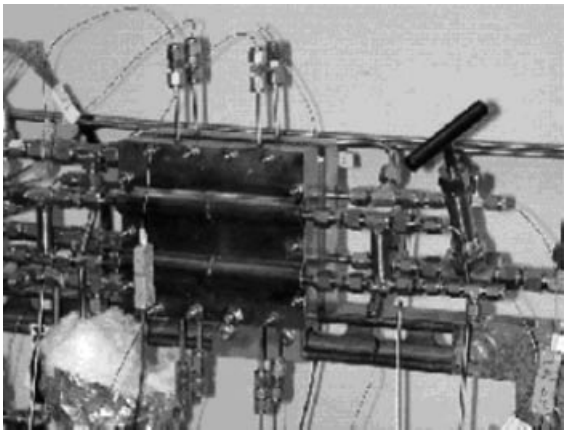

**Figure 27.15** Prototype 2 $kW_e$ PrOx reactor with microchannels for quasi-isothermal operation.

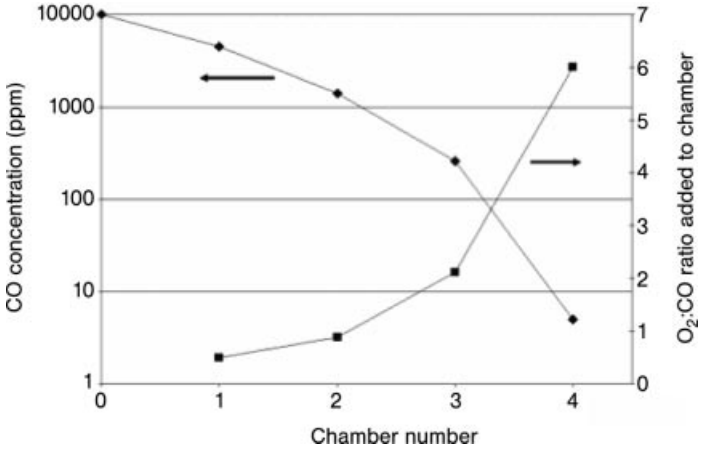


**Figure 27.16** Decrease of CO concentration from chamber to chamber through the OrIx reactor with 1% inlet CO concentration and a steam to carbon ratio of 0.3.

## 27.4
## A Detailed Example: A Thin-film Catalytic Microreactor as a Kinetic Tool

A detailed example is included here to evaluate thin-film catalytic microreactors as kinetic tools compared with conventional laboratory reactors. Most kinetic studies carried out in laboratory reactors which utilize small catalyst particles and the intrinsic kinetics for rapid reactions could be well hidden by mass and heat transport limitations. Existing criteria for mass and heat transport were estimated for both a microreactor with a thin-film catalyst thickness of 5 μm and a packed-bed laboratory reactor with radii of 2 and 4 mm [22]. Based on the calculation of Weitz–Prater

parameters for internal mass transport and the overall specific reaction rates for external mass transport, both types of reactors show negligible internal and external mass transport resistance under typical PrOx operating temperatures of 160–220 °C. On the other hand, an estimate of the Damköhler number (*Da*) for intraparticle heat transport indicated strong limitations for the conventional packed-bed reactor in which the catalyst thickness (i.e. radius for the packed bed or thickness of the catalyst layer for the microreactor) is the determining factor. The equivalent thickness of the thin-film catalyst of the microreactor is several orders of magnitude smaller than that for the packed-bed catalyst. Due to the quadratic dependence of *Da* on the catalyst thickness, *Da* of the packed-bed is more than five orders of magnitude greater than that for the microreactor, which suggests severe heat transport limitations for the packed bed for the highly exothermic PrOx reaction. In order to study quantitatively intrinsic reaction kinetics and the effect of transport limitations on kinetic assessment, a comprehensive method, integrating micro-kinetic reaction simulation and 3D non-isothermal reactor design, was developed to adapt to our experimental study of a silicon microchannel reactor with a $Pt/Al_2O_3$ thin-film wall catalyst.

### 27.4.1 Experimental

Silicon chips used in this study were fabricated with conventional photolithography and deep reactive ion etching (DRIE) processes. As many as 40 devices were formed on an 8 inch wafer and then sawn to obtain individual chips. The reactors were closed by anodic bonding of the silicon chip to a piece of Pyrex glass, before or after catalyst incorporation in the microchannel. The finished chips have the same configuration of two inlets for the introduction of air and simulated reformate, a premixer, a single channel with immobilized thin-film catalyst, a cooling channel for reaction quenching and an outlet (Figure 27.17). All reactors considered had dimensions of 500 μm (width) × 470 μm (depth) × 4.5 cm (length). More details on the microreactor fabrication have been published elsewhere [48]. The thin-film $Pt/Al_2O_3$ catalyst was synthesized using a sol–gel technique as described elsewhere [49]. For reaction characterization, three reactant gases were used: mixture 1, which was a simulated reformate (1.7% CO, 68.0% $H_2$, 21.0% $CO_2$ and $N_2$ as balance), mixture 2 (1.7% CO, 21.0% $CO_2$ and inert) and dry air (78.1% $N_2$ and 21.9% $O_2$).


**Figure 27.17** Si microchannel reactor with channel dimensions of 500 μm (width) × 610 μm (depth) × 4.5 cm (length).

### 27.4.2 Microkinetic Reaction Simulation

A microkinetic reaction model was constructed to elucidate the intrinsic reaction mechanism and to provide insight into the processes occurring in the reactor. CHEMKIN software [50] was used to accommodate this model. The PrOx reaction mechanism describing the detailed gas-phase and surface chemical kinetics was constructed from previously published work [51] and adapting the rate parameters to our experimental results. The model is composed of eight adsorption reactions, eight desorption reactions and 12 surface reactions with nine gas-phase species ($N_2$, O, $O_2$, $CO_2$, H, OH, CO, $H_2$, $H_2O$) and eight surface species [Pt(s), O(s), H(s), OH(s), $H_2O$(s), C(s), CO(s), $CO_2$ (s)].

Upon completion of the reaction model, the CHEMKIN software provides information on rates of production of various species from each reaction, along with measures of the sensitivity of the solution to each reaction rate. Such an analysis facilitated the assessment of reaction importance and resulted in the reaction network in Figure 27.19, which shows the nine major forward and reverse reactions that comprise the overall reaction pathways for consumption of CO and formation of $H_2O$ and $CO_2$ for the conditions of interest. The reaction model was thus verified with established PrOx mechanisms in the literature and compared with our experimental data.

The identification of $O_2$ adsorption as the rate-limiting step at low temperatures has been substantiated experimentally in various studies [4, 6, 8, 19]. In our model, $O_2$ adsorption is also identified as the rate-limiting step (step 2 in Figure 27.18) in the sequence of surface reactions for $CO_2$ production. Among the major adsorption reactions (reactions 1–4), CO adsorption (reaction 3) has the highest sticking coefficient along with a relatively slow desorption rate. This results in CO(s) surface domination before reaching the light-off temperature and subsequently limits the $O_2$ adsorption and the CO(s) oxidation. At temperatures that reach light-off, the CO desorption rate increases, which opens up enough Pt sites for $O_2$ adsorption and the onset of CO(s) oxidation. In addition, $H_2O$ formation is negligible at low temperatures, being limited by the low H(s) and O(s) coverage. The onset of CO(s) oxidation at higher temperature sharply reduces CO(s) coverage and fast desorption of $CO_2$(s) permits H(s) and O(s) concentrations to increase along with the subsequent $H_2O$(s) production.

Another mechanism studied is the $CO_2$ production pathway in PrOx. The importance of the surface hydroxyl species on PrOx reaction activity has been reported [52, 53] and found to be formed by the addition of either $H_2$ [10, 12] or $H_2O$ [11, 26] in the reactant stream. Our modeling results also suggest that the addition of $H_2$ increases the rate of CO oxidation by facilitating the formation of surface hydroxyl species. In Figure 27.1, our model shows two pathways for $CO_2$ formation: step 4 and steps 5 and 6. As indicated by the higher net-rate values, the latter path through the formation of OH(s) is the major path for $CO_2$(s) production. In order to corroborate this mechanism and its effect, experiments were conducted using two reactant mixtures, one without and a second with $H_2$ (Figure 27.19). The

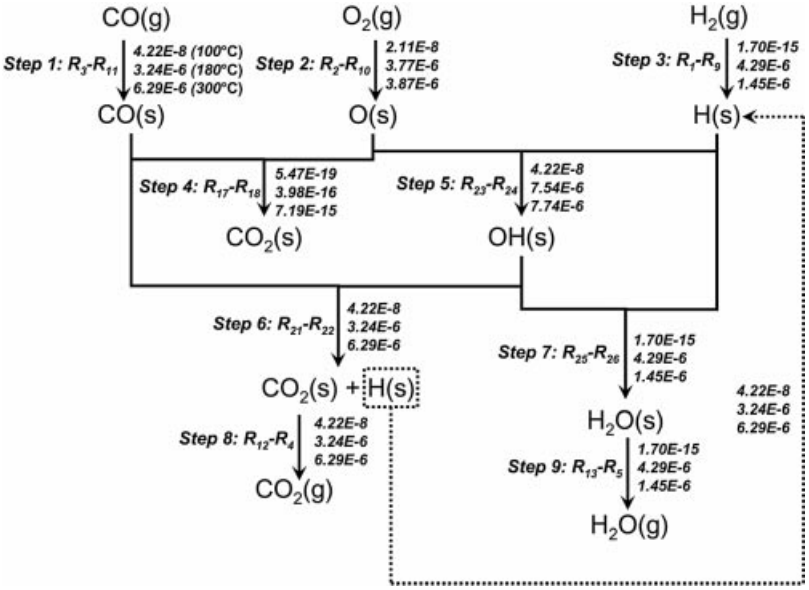


**Figure 27.18** Elementary reaction network showing the pathways involving $CO_2$, $H_2O$ and CO. Steady-state reaction rates (mol $s^{-1}$) in the whole microreactor at 100, 180 and 300 °C are also shown. WHSV = 1500 $h^{-1}$; flow rate (mixture 1) = 5.0 N $cm^3$ $min^{-1}$; flow rate (air) = 0.5 N $cm^3$ $min^{-1}$.

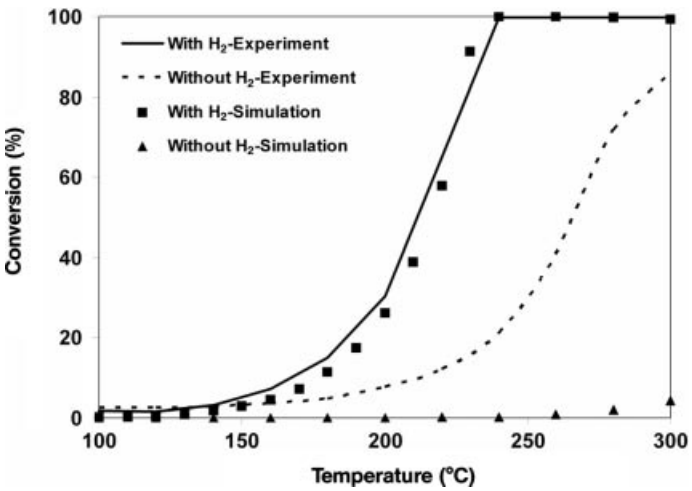


**Figure 27.19** Experimental and simulation results indicate that the addition of $H_2$ significantly increases CO conversion. WHSV = 11 000 $h^{-1}$; flow rate (mixture 1 or 2) = 5.0 N $cm^3$ $min^{-1}$; flow rate (air) = 0.5 N $cm^3$ $min^{-1}$.

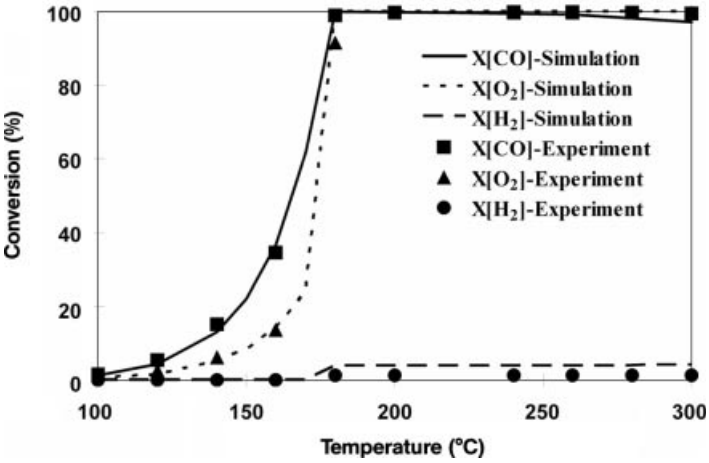


**Figure 27.20** CHEMKIN simulation agreed well with experimental results for $X_{CO}$, $X_{O_2}$ and $X_{H_2}$.WHSV = 1500 $h^{-1}$; flow rate (mixture 1) = 5.0 N $cm^3$ $min^{-1}$; flow rate (air) = 0.5 N $cm^3$ $min^{-1}$.

experimental results agree qualitatively with the literature and our simulation that the light-off slope shifts to lower temperature with $H_2$ in the reactant stream at the temperatures before and during light-off.

With verification of the above reaction mechanisms, the CHEMKIN model was then used to predict the experimental results of CO conversion and $CO_2$ selectivity in the microreactor (Figure 27.20). As discussed previously, the catalyst active sites in the model are dominated by CO(s) before light-off. $CO_2$ is produced preferentially to $H_2O$ before CO light-off. As a result, CO conversion increases slightly with no appreciable $H_2$ conversion below light-off. However, at higher temperatures during and after light-off, the CO(s) coverage drops steadily due to the increased CO(s) desorption rate and the onset of CO(s) oxidation, allowing a concomitant increase in H(s) mole fraction. The rate of $H_2O$ formation then rises substantially, accompanied by a decline in $CO_2$ selectivity.

In summary, the combination of experimental studies and detailed chemical kinetic simulations provides a more complete picture of surface kinetics and identifies new regions of parameter space that would offer higher efficiency.

### 27.4.3
### Quasi–3D Non-isothermal Reactor Model

The qualitative analysis of intraparticle heat transport suggests severe limitations of packed-bed laboratory reactors compared with the thin-film catalyzed microchannel, as discussed previously. It is imperative that a quantitative study of reactor heat transfer limitations is performed. With PrOx as a model reaction, this study was realized through the non-isothermal reactor modeling of the microreactor and the packed-bed reactors with both 2 and 4 mm radii. In the model, the operating

temperature (i.e. the silicon substrate temperature) was assumed to be isothermal due to the high thermal conductivity and large thermal mass of the silicon substrate and the active cooling through the microchannel passageway.

The modeling results of the microreactor with $5 \times 10^{-6}$ m catalyst film shows an essentially isothermal temperature distribution in the thin-film catalyst of the microreactor, even at the highest operating temperature (300 °C), supporting our qualitative analysis. On the other hand, the modeling results for the 2 mm packed bed show significant temperature gradients, as indicated by Figure 27.21. The temperature gradients become more dramatic and move upstream with higher isothermal wall temperatures, which suggest large accumulated reaction heat caused by inefficient heat transfer within the reactor. Figure 27.22 plots the 2 mm packed-bed modeling results of $O_2$, CO, $H_2$ conversions and $CO_2$ selectivity along the reactor. When the wall temperature increases, full conversion of $O_2$ (with CO and $H_2$) takes place in shorter reactor lengths, implying a higher density of heat accumulation and consequently larger temperature gradients in the region with the most oxidation activity.

Further insight into the modeling results can be given as follows. Due to the low $O_2$ reaction activity (Figure 27.22a) at low temperatures (e.g. $T_w = 120$ °C), the temperature gradient is negligible in both the axial and radial directions, as shown in Figure 27.21a. At 180 °C, the $O_2$ reaction activity is mild up to $l = 2 \times 10^{-2}$ m (Figure 27.22b), which leads to small temperature gradients in this region (Figure 27.21b). However, as also indicated by Figure 27.22b, the sudden increase in both CO and $H_2$ oxidation activity between $l = 2 \times 10^{-2}$ and $2.5 \times 10^{-2}$ m causes a dramatic increase in accumulated reaction heat, leading to temperatures much higher internally than at the wall (Figure 27.21b). With further increase in the wall temperature, more severe temperature gradients are developed close to the entrance of the reactor (Figure 27.21c), since full $O_2$ conversion is reached at a length of only $10^{-3}$ m (Figure 27.22c).

Figure 27.23 plots the modeling results of CO conversion at different wall temperatures for the microreactor and the 2 and 4 mm packed beds. As discussed above, the microreactor displays a uniform temperature distribution, resulting in a CO conversion curve coinciding nearly exactly with the result for ideal isothermal operation. In contrast, the results for the packed beds show different characteristic curves driven by the temperature gradients and the resulting local reaction activities for all three PrOx reactions (Equations 27.1–27.3). Particularly at higher temperatures, the drop in the CO conversion for the packed beds is caused by strong r-WGS conversion activated by high local temperatures in these reactors. This phenomenon is seen to intensify as the radial thermal resistance increases (4 versus 2 mm).

The extremely efficient heat removal of the thin-film catalyst in the smaller cross-section microchannel virtually eliminates any temperature gradients, which are essentially inevitable for conventional packed-bed reactors. The temperature gradients in the packed-bed reactors then favor the r-WGS reaction and a narrow operating temperature window. This study also suggests the advantage of the utility of the microreactor for accessing intrinsic reaction kinetics compared with packed-bed reactors.

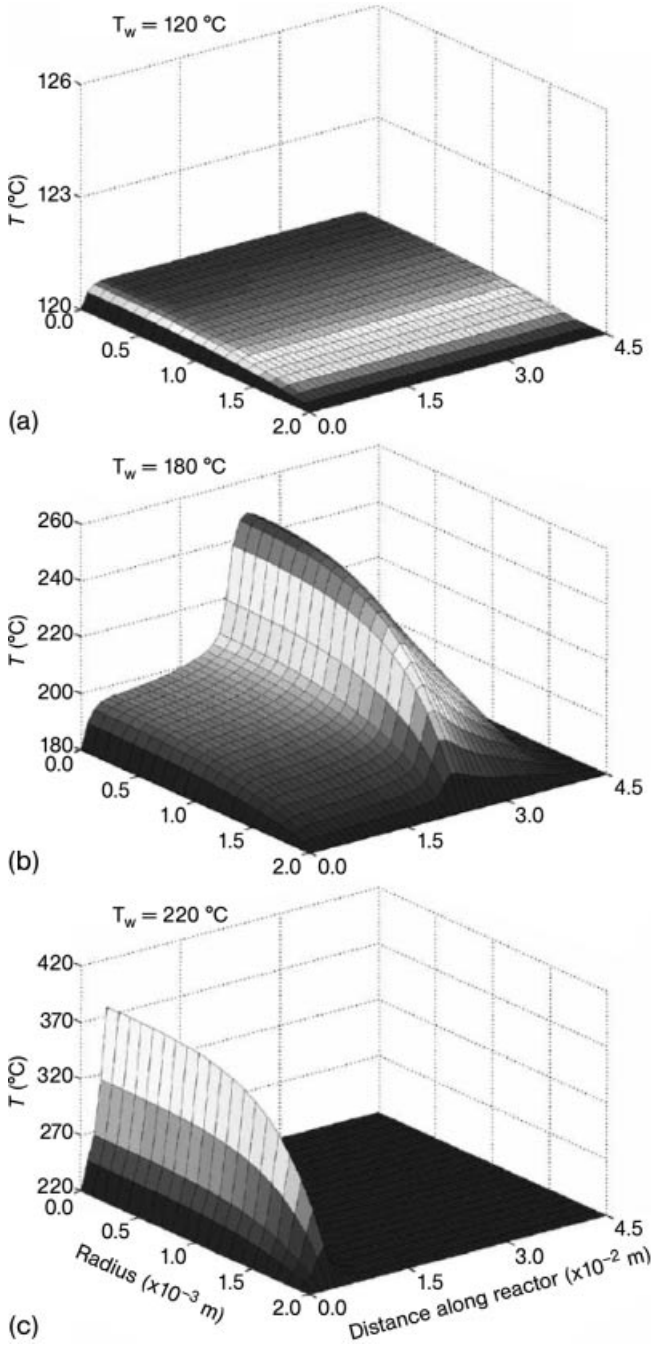


**Figure 27.21** Plots of reactor temperature distribution for the 2 mm packed bed with $T_w = 120$, 180 and 220 °C. WHSV = 1500 $h^{-1}$.

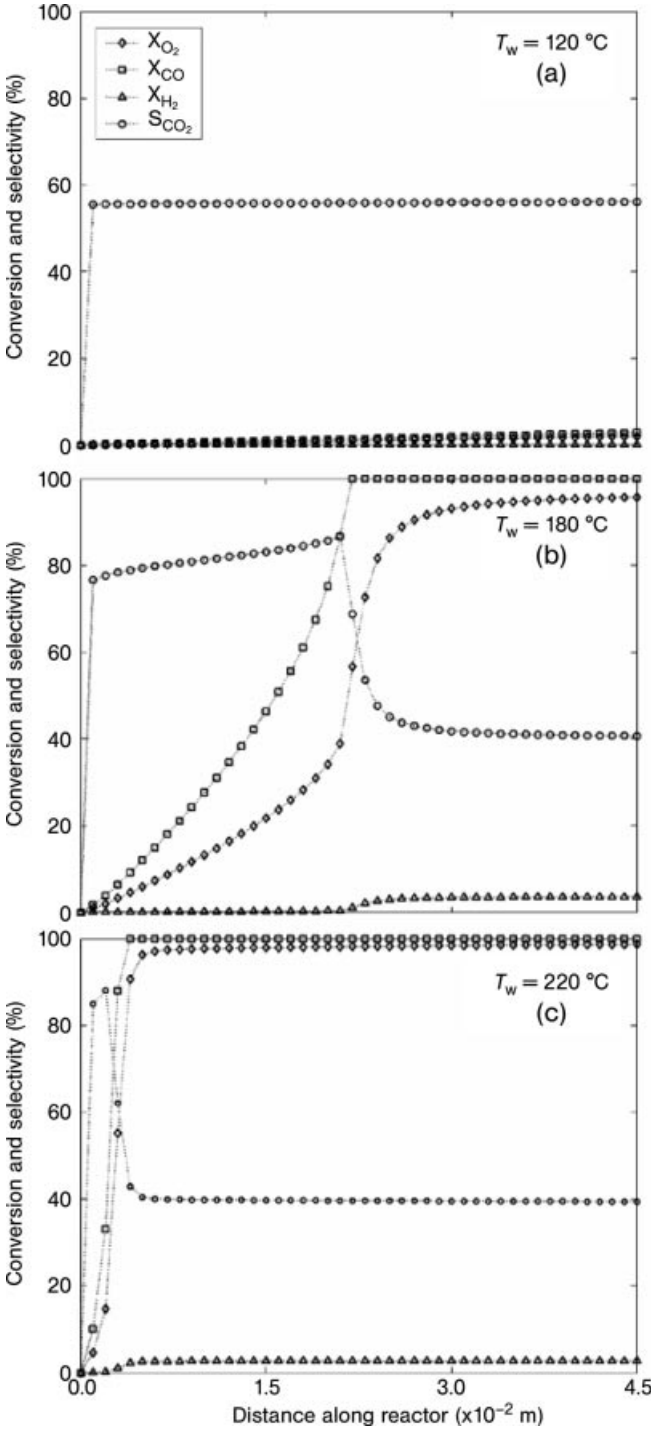


**Figure 27.22** $O_2$, CO, $H_2$ conversion and $CO_2$ selectivity along the reactor length of 2 mm packed bed with $T_w = 120$, 180 and 220 °C. WHSV = 1500 $h^{-1}$.

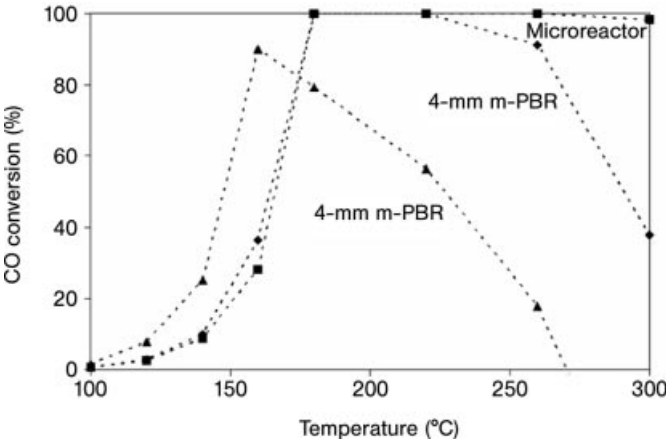


**Figure 27.23** CO conversion versus reactor wall temperature for the microreactor, 2 and 4 mm packed beds. WHSV = 1500 $h^{-1}$.

## 27.5 Conclusion

The design of a PrOx reactor requires superior heat transfer properties due to the rapid kinetics and strong exothermicity intrinsic to this reaction system. The research work of different groups has demonstrated that microreactors with thin-film catalysts perform better than conventional packed-bed systems with suppressed hot-spot formation and wider operating temperature windows. With this benefit from the microreactors, other research studies have shown microreactors to be a promising platform to design fuel processors with high integration, compactness and scale-up capability. Further, a detailed example indicated that the advantage of thin-film catalytic microreactors for this type of reactions lies in their extremely short heat transfer length.

## References


1 Q. Qi, B. Peppley, K. Karan, Integrated fuel processors for fuel cell application: a review. *Fuel Process. Technol.* **2007**, *88*, 3–22.

2 M. Echigo, T. Tabata, CO removal from reformed gas by catalytic methanation for polymer electrolyte fuel cell applications. *J. Chem. Eng. Jpn.* **2004**, *37*, 75–81.

3 G. Xu, X. Chen, Z. G. Zhang, Temperature-staged methanation: an alternative method to purify hydrogen-rich fuel gas for PEFC. *Chem. Eng. J.* **2006**, *121*, 97–107.

4 M. J. Kahlich, H. A. Gasteiger, R. J. Behm, Kinetics of the selective CO oxidation in $H_2$-rich gas on $Pt/Al_2O_3$. *J. Catal.* **1997**, *171*, 93–105.

5 Y. Choi, H. G. Stenger, Kinetics, simulation and insights for CO selective oxidation in fuel cell applications. *J. Power Sources* **2004**, *129*, 246–254.

**6** S. H. Oh, R. M. Sinkevitch, Carbon monoxide removal from hydrogen-rich fuel cell feedstreams by selective catalytic oxidation. *J. Catal.* **1993**, *142*, 254–262.

**7** M. J. Castaldi, R. S. Boorse, S. Roychoudhury, P. V. Menacherry, W. C. Pfefferle, A compact lightweight, fast-response preferential oxidation reactor for PEM automotive fuel cell applications, in *Proceedings of the National Science Foundation's Annual SBIR/STTR Meeting*, San Juan, Puerto Rico, **2002**, www.precision-combustion.com/proxpaper.pdf (accessed 10 September 2003).

**8** A. Manasilp, E. Gulari, Selective CO oxidation over Pt/alumina catalysts for fuel cell applications. *Appl. Catal. B* **2002**, *37*, 17–25.

**9** E. J. Bissett, S. H. Oh, R. M. Sinkevitch, Pt surface kinetics for a PrOx reactor for fuel cell feedstream processing. *Chem. Eng. Sci.* **2005**, *60*, 4709–4721.

**10** G. S. Zafiris, R. J. Gorte, CO oxidation on Pt/$\alpha$-$Al_2O_3$(0001): evidence for structure sensitivity. *J. Catal.* **1993**, *140*, 418–423.

**11** I. H. Son, M. Shamasuzzoha, A. M. Lane, Promotion of Pt/$\gamma$-$Al_2O_3$ by new pretreatment for low-temperature preferential oxidation of CO in $H_2$ for PEM fuel cells. *J. Catal.* **2002**, *210*, 460–465.

**12** O. Korotkikh, R. Farrauto, Selective catalytic oxidation of CO in $H_2$: fuel cell applications. *Catal. Today* **2000**, *62*, 249–254.

**13** X. Liu, O. Korotkikh, R. Farrauto, Selective catalytic oxidation of CO in $H_2$: structural study of Fe oxide-promoted Pt/alumina catalyst. *Appl. Catal. A* **2002**, *226*, 293–303.

**14** G. W. Roberts, P. Chin, X. L. Sun, J. J. Spivey, Preferential oxidation of carbon monoxide with Pt/Fe monolithic catalysts: interactions between external transport and the reverse water-gas-shift reaction. *Appl. Catal. B* **2003**, *46*, 601–611.

**15** Y. F. Han, M. Kinne, R. J. Behm, Selective oxidation of CO on Ru/$\gamma$-$Al_2O_3$ in methanol reformate at low temperatures. *Appl. Catal. B* **2004**, *52*, 123–134.

**16** T. V. Choudhary, D. W. Goodman, CO oxidation on supported nano-Au catalysts synthesized from a $[Au_6(PPh_3)_6](BF_4)_2$ complex. *J. Catal.* **2002**, *207*, 247–255.

**17** H. H. Kung, M. C. Kung, C. K. Costello, Supported Au catalysts for low temperature CO oxidation. *J. Catal.* **2003**, *216*, 425–432.

**18** Y. Teng, H. Skurai, A. Ueda, T. Kobayashi, Oxidative removal of CO contained in hydrogen by using metal oxide catalysts. *Int. J. Hydrogen Energy* **1999**, *24*, 355–358.

**19** G. Avgouropoulos, T. Ioannides, Ch. Papadopoulou, J. Batista, S. Hocevar, H. K. Matralis, A comparative study of Pt/$\gamma$-$Al_2O_3$, Au/$\alpha$-$Fe_2O_3$ and CuO–$CeO_2$ catalysts for the selective oxidation of carbon monoxide in excess hydrogen. *Catal. Today* **2002**, *75*, 157–167.

**20** S. K. Ajmera, C. Delattre, M. A. Schmidt, K. F. Jensen, Microfabricated differential reactor for heterogeneous gas phase catalyst testing. *J. Catal.* **2002**, *209*, 401–412.

**21** D. H. Kim, M. S. Lim, Kinetics of selective CO oxidation in hydrogen-rich mixtures on Pt/alumina catalysts. *Appl. Catal. A* **2002**, *224*, 27–38.

**22** X. Ouyang, L. Bednarova, P. Ho, R. S. Besser, PrOx in a thin-film catalytic microreactor: advantages and limitations. *AIChE J.* **2005**, *51*, 1758–1772.

**23** S. H. Lee, J. Han, K. Y. Lee, Development of 10-kWe preferential oxidation system for fuel cell vehicles. *J. Power Sources* **2002**, *109*, 394–402.

**24** X. Ouyang, R. S. Besser, Effect of reactor heat transfer limitations on CO preferential oxidation. *J. Power Sources* **2004**, *141*, 39–46.

**25** M. J. Kahlich, H. A. Gasteiger, R. J. Behm, Kinetics of the selective CO oxidation in $H_2$-rich gas on Pt/$Al_2O_3$. *J. Catal.* . **1997**, *171*, 93–105.

**26** R. H. Nibbelke, M. A. J. Campman, J. H. B. J. Hoebink, G. B. Marin, Kinetic study of the CO oxidation over Pt/$\gamma$-$Al_2O_3$ and Pt/Rh/$CeO_2$/$\gamma$-$Al_2O_3$ in the presence of $H_2O$ and $CO_2$. *J. Catal.* **1997**, *171*, 358–373.

**27** D. H. Kim, M. S. Lim, Kinetics of selective CO oxidation in hydrogen-rich mixtures on Pt/alumina catalysts. *Appl. Catal. A* **2002**, *224*, 27–38.

**28** E. J. Bissett, S. H. Oh, R. M. Sinkevitch, Pt surface kinetics for a PrOx reactor for fuel cell feedstream processing. *Chem. Eng. Sci.* **2005**, *60*, 4709–4721.

**29** Y. Choi, H. G. Stenger, Kinetics, simulation and insights for CO selective oxidation in fuel cell applications. *J. Power Sources* **2004**, *129*, 246–254.

**30** R. H. Venderbosch, W. Prins, W. P. M. van Swaajj, Platinum catalyzed oxidation of carbon monoxide as a model reaction in mass transfer measurement. *Chem. Eng. Sci.* **1998**, *53*, 3355–3366.

**31** Y. Choi, H. G. Stenger, Water gas shift reaction kinetics and reactor modeling for fuel cell grade hydrogen. *J. Power Sources* **2003**, *124*, 432–439.

**32** J. M. Moe, Design of water-gas shift reactors. *Chem. Eng. Prog.* **1962**, *58*, 33–36.

**33** G. Kolb, V. Hessel, V. Cominos, *et al.* Selective oxidations in micro-structured catalytic reactors—For gas-phase reactions and specifically for fuel processing for fuel cells. *Catal. Today* **2007**, *120*, 2–20.

**34** V. Cominos, V. Hessel, C. Hofmann, *et al.* Selective oxidation of carbon monoxide in a hydrogen-rich fuel cell feed using a catalyst coated microstructured reactor. *Catal. Today* **2005**, *110*, 140–153.

**35** E. R. Delsman, E. V. Rebrov, M. H. J. M. De Croon, *et al.* MiRTH-e: micro reactor technology for hydrogen and electricity, in *Proceedings of the Fifth International Conference on Microreaction Technology*, Springer, Berlin, **2001**, 268–274.

**36** S. Srinivas, A. Dhingra, H. Im, A scalable silicon microreactor for preferential CO oxidation: performance comparison with a tubular packed-bed microreactor. *Appl. Catal. A* **2004**, *274*, 285–293.

**37** G. Chen, Q. Yuan, H. Li, *et al.* CO selective oxidation in a microchannel reactor for PEM fuel cell. *Chem. Eng. J.* **2004**, *101*, 101–106.

**38** O. Goerke, P. Pfeifer, K. Schubert, Water gas shift reaction and selective oxidation of CO in microreactors. *Appl. Catal. A* **2004**, *263*, 11–18.

**39** G. Avgouropoulos, T. Ioannides, C. Papadopoulou, *et al.* A comparative study of Pt/$\gamma$-$Al_2O_3$, Au/$\alpha$-$Fe_2O_3$ and CuO-$CeO_2$ catalysts for the selective oxidation of carbon monoxide in excess hydrogen, *Catal. Today* **2002**, 75, 157–167.

**40** C. D. Dudfield, R. Chen, P. L. Adcock, A compact CO selective oxidation reactor for solid polymer fuel cell powered vehicle application, *J. Power Sources* **2000**, 86, 214–222.

**41** Y. Kawamura, N. Ogura, T. Yahata, *et al.* Multi-layered microreactor system with methanol reformer for small PEMFC, *J. Chem. Eng. Jpn.* **2005**, *38*, 854–858.

**42** T. Yahata, K. Takeyama, S. Nakayama, Hydrogen production by methanol reforming with a thermally optimized microreactor for a small PEMFC system, presented at Fuel Cell Seminar 2006, Honolulu, Hawaii, **2006**.

**43** N. Miyamoto, T. Yahata, T. Fujita, *et al.* Development of a thermally efficient microreactor with a methanol reformer for small PEMFC systems, presented at Fuel Cell Seminar 2006, Honolulu, Hawaii, **2006**.

**44** E. R. Delsman, M. H. J. M. De Croon, A. Pierik, *et al.* Design and operation of a preferential oxidation microdevice for a portable fuel processor. *Chem. Eng. Sci.* **2004**, *59*, 4795–4802.

**45** E. R. Delsman, M. H. J. M. De Croon, G. J. Kramer, *et al.* Experiments and modeling of an integrated preferential oxidation–heat exchanger microdevice. *Chem. Eng. J.* **2004**, *101*, 123–131.

**46** L. Thompson, Fuel processors for PEM fuel cells, http://www.hydrogen.energy.gov/pdfs/progress04/ivf2_thompson.pdf (accessed 5 February 2007).

**47** W. TeGrotenhuis, K. Brooks, R. Dagle, *et al.* Microchannel reformate cleanup: water

gas shift and preferential oxidation, http://www.hydrogen.energy.gov/pdfs/progress04/ivf3_tegrotenhuis.pdf (accessed 5 February 2007).

**48** H. Surangalikar, X. Ouyang, R. S. Besser, Experimental study of hydrocarbon hydrogenation and dehydrogenation reactions in silicon microfabricated reactors of two different geometries. *Chem. Eng. J.* **2003**, *93*, 217–224.

**49** H. Chen, L. Bednarova, R. S. Besser, *et al.* Surface-selective infiltration of thin-film catalyst intomicrochannel reactors. *Appl. Catal. A* **2005**, *286*, 186–195.

**50** R. J. Kee, F. M. Rupley, J. A. Miller, *et al. Chemkin Collection, Release 3.7.1*, Reaction Design, San Diego, CA, **2003**.

**51** D. K. Zerkle, M. D. Allendorf, M. Wolf, O. Deutschmann, Understanding homogeneous and heterogeneous contributions to the platinum-catalyzed partial oxidation of ethane in a short-contact-time reactor. *J. Catal.* **2000**, *196*, 18–39.

**52** M. M. Schubert, H. A. Gasteiger, R. J. Behm, Research note: surface formates as side product in the selective CO oxidation on Pt/$\gamma$-$Al_2O_3$. *J. Catal.* **1997**, *172*, 256–258.

**53** A. B. Mhadeshwar, D. G. Vlachos, Microkinetic modeling for water-promoted CO oxidation, water-gas shift and preferential oxidation of CO on Pt. *J. Phys. Chem. B* **2004**, *108*, 15246–15258.